Electronic Supplementary Information (ESI)

Ion engine in hydrogels boosting hydrovoltaic electricity generation

Nan He, Haonan Wang, Fan Li, Bo Jiang, Dawei Tang, Lin Li*

Key Laboratory of Ocean Energy Utilization and Energy Conservation of Ministry of Education, School of energy and power engineering, Dalian University of Technology, Dalian, Liaoning 116024, P. R. China.

Correspondence to: lilinnd@dlut.edu.cn

The detailed material reparation for hydrogels with various kinds of IGC

None-IGC HEG: x mmol NaAMPS, 3 g AAM, 0.0037 g MBAA, 0.0054 g UV-I, and 0.2019 g AG were mixed in 7 mL DI water. According to the designed none IGC distribution, the x was 0 in Solution 1, Solution 2, Solution 3, and Solution 4. Then the solutions were stirred on a magnetic stirrer under 50℃ heating and 500 rpm for 10 min, respectively. The hot and clear solution 1, solution 2, solution 3, and solution 4 were successively poured into the mould in equal parts. Then set for about 30 min, ensuring that the solution is cool and copolymerisation occurs. The pre-hydrogel was irradiated with 365 nm ultraviolet light under 45 W of irradiation power for an hour. To obtain a smooth and flat hydrogel, a glass sheet was employed to cover the surface of the pre-gel before UV irradiation tightly.

All-IGC HEG: x mmol NaAMPS, 3 g AAM, 0.0037 g MBAA, 0.0054 g UV-I, and 0.2019 g AG were mixed in 7 mL DI water. According to the designed all IGC distribution, the x was 2.4 in Solution 1, Solution 2, Solution 3, and Solution 4. Then the solutions were stirred on a magnetic stirrer under 50℃ heating and 500 rpm for 10 min, respectively. The hot and clear solution 1, solution 2, solution 3, and solution 4 were successively poured into the mould in equal parts. Then set for about 30 min, ensuring that the solution is cool and copolymerisation occurs. The pre-hydrogel was irradiated with 365 nm ultraviolet light under 45 W of irradiation power for an hour. To obtain a smooth and flat hydrogel, a glass sheet was employed to cover the surface of the pre-gel before UV irradiation tightly.

Weak-IGC gradient HEG: x mmol NaAMPS, 3 g AAM, 0.0037 g MBAA, 0.0054 g UV-I, and 0.2019 g AG were mixed in 7 mL DI water. According to the designed gradient distribution, the x was 2.4 in Solution 1, 1.2 in Solution 2, and 0.6 in Solution 3. 1.7 g AAM, 0.0019 g MBAA, 0.0054 g UV-I, and 0.1622 g AG were mixed in 7 mL DI water (Solution 4 and 5). Then the solutions were stirred on a magnetic stirrer under 50℃ heating and 500 rpm for 10 min, respectively. The hot and clear solution 1, solution 2, solution 3, and solution 4 were successively poured into the left half of the mould in equal parts. The hot and clear solution 5 was then poured into the right half of the mould. Then set for about 30 min, ensuring that the solution is cool and copolymerisation occurs. The pre-hydrogel was irradiated with 365 nm ultraviolet light under 45 W of irradiation power for an hour. To obtain a smooth and flat hydrogel, a glass sheet was employed to cover the surface of the pre-gel before UV irradiation tightly.

Strong-IGC gradient HEG: x mmol NaAMPS, 3 g AAM, 0.0037 g MBAA, 0.0054 g UV-I, and 0.2019 g AG were mixed in 7 mL DI water. According to the designed gradient distribution, the x was 2.4 in Solution 1, 1.2 in Solution 2, and 0.6 in Solution 3. 1.7 g AAM, 0.0019 g MBAA, 0.0054 g UV-I, and 0.1622 g AG were mixed in 7 mL DI water (Solution 4). Then the solutions were stirred on a magnetic stirrer under 50℃ heating and 500 rpm for 10 min, respectively. The hot and clear solution 1, solution 2, solution 3, and solution 4 were successively poured into the mould in equal parts. Then set for about 30 min, ensuring that the solution is cool and copolymerisation occurs. The pre-hydrogel was irradiated with 365 nm ultraviolet light under 45 W of irradiation power for an hour. To obtain a smooth and flat hydrogel, a glass sheet was employed to cover the surface of the pre-gel before UV irradiation tightly.

Supplementary Figures and Tables

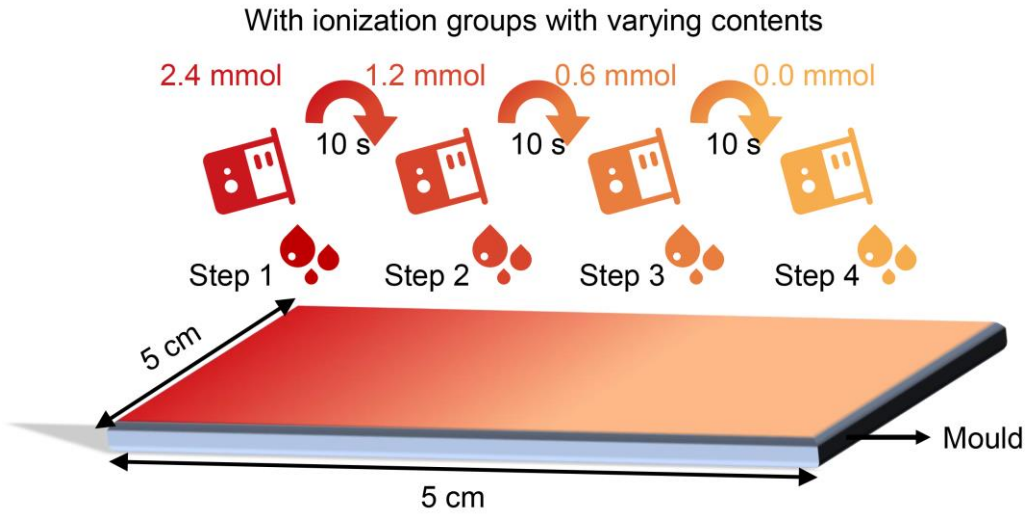

Fig. S1 Schematic diagram of the successive pouring method.

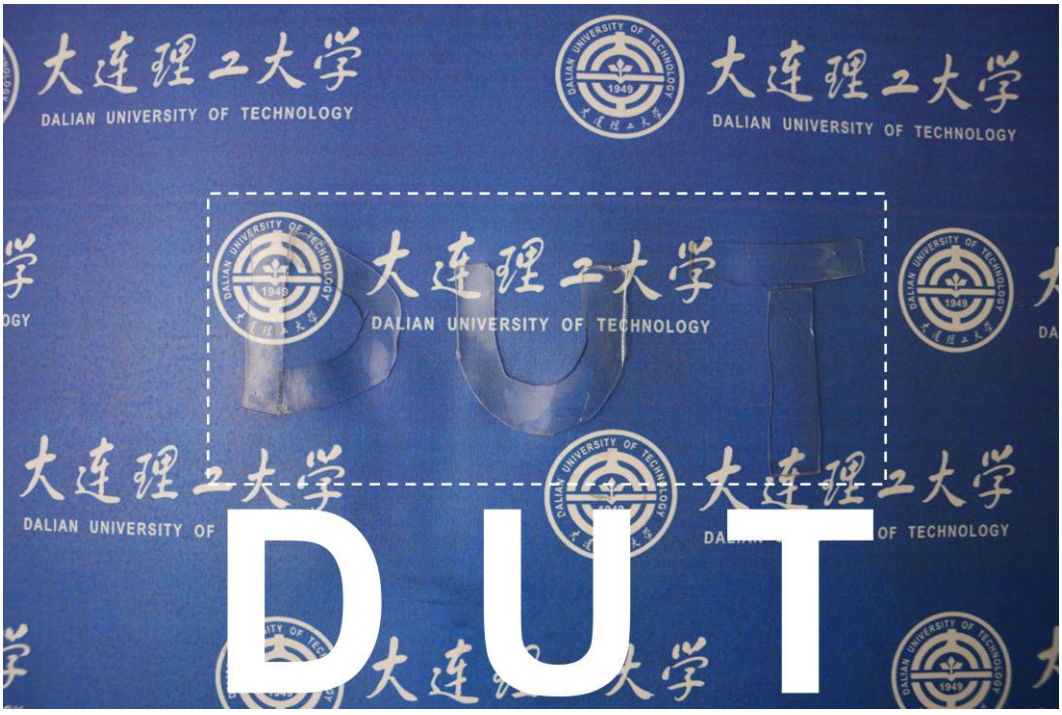

Fig. S2 Photo of the tailored ion-engine HEG.

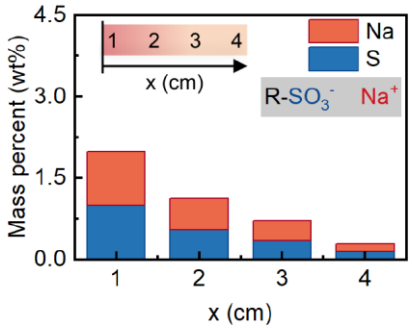

Fig. S3 Corresponding semi-quantitative analysis from EDS mapping.

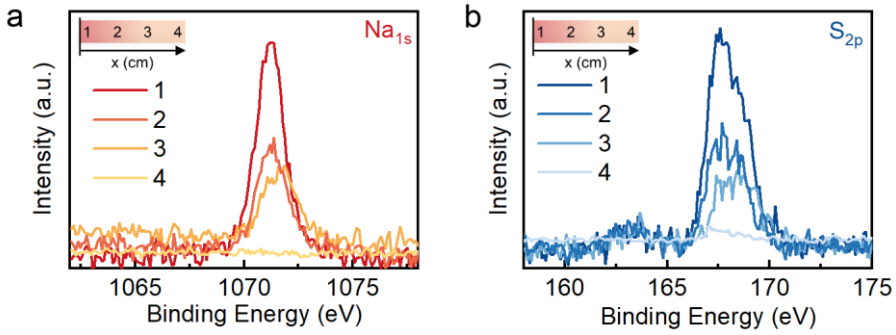

Fig. S4 X-ray photoelectron spectroscopy (XPS) spectra characterising the feature elements of ionisation group, i.e., -SO_3Na, distributed in four regions along the gradient.

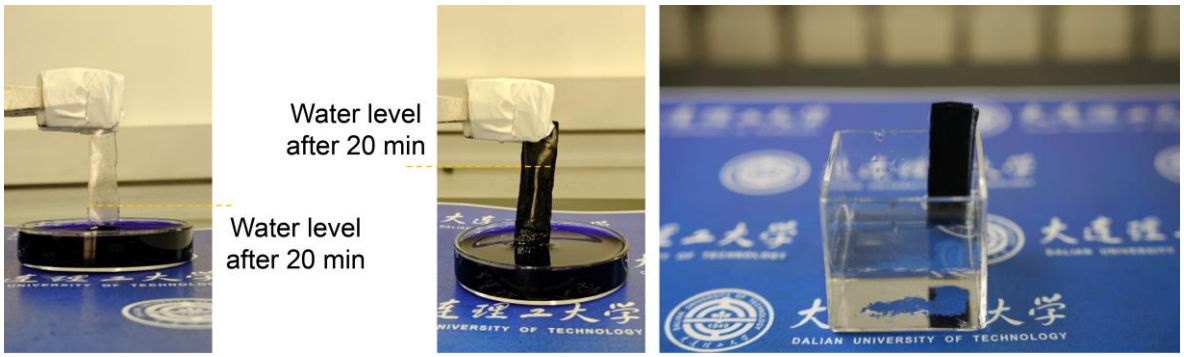

Fig. S5 Water level of water absorbing without and with a conductive carbon fibre after 20 min.

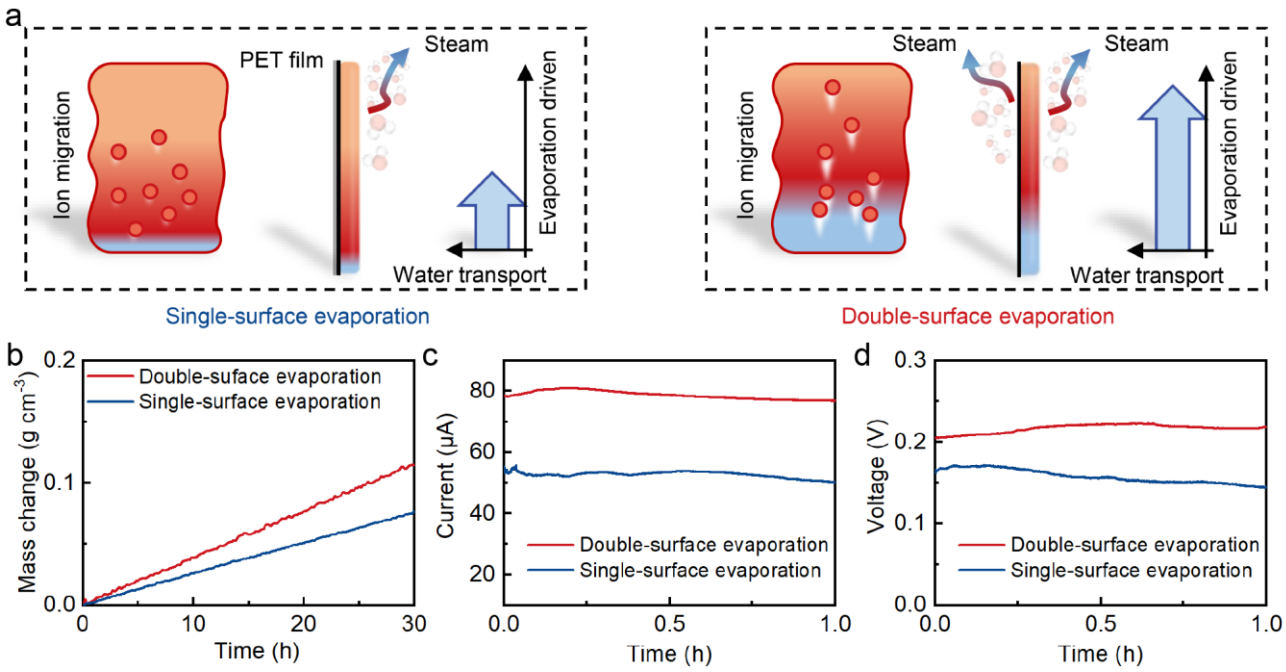

Fig. S6 Analysis of the effect of water evaporation capacity on electric output. (a) Schematic mechanism that increasing evaporation area to enhance water evaporation capacity, thus improving water transport and ion migration for a high performance of electric performance. (b–d) Evaporated water mass change, short-circuit current, and open-circuit voltage of the single-surface evaporation configuration and the double-surface evaporation configuration. Note that in single-surface evaporation, the side of the carbon fibre was completely sealed.

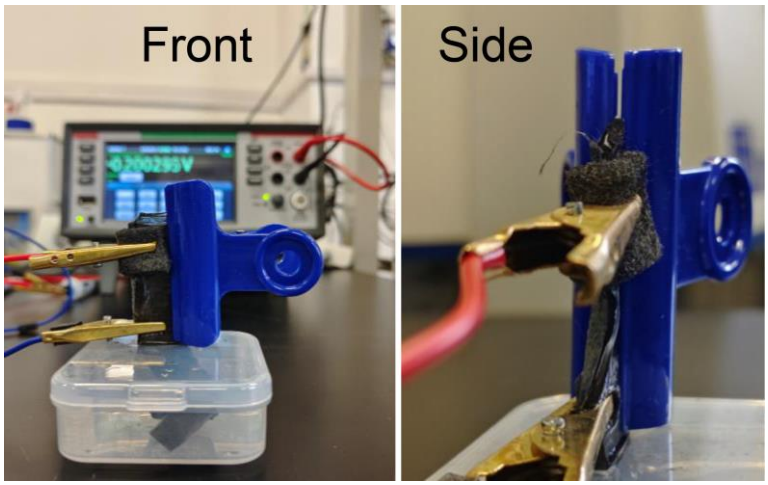

Fig. S7 Photos of the front and side of the measurement unit.

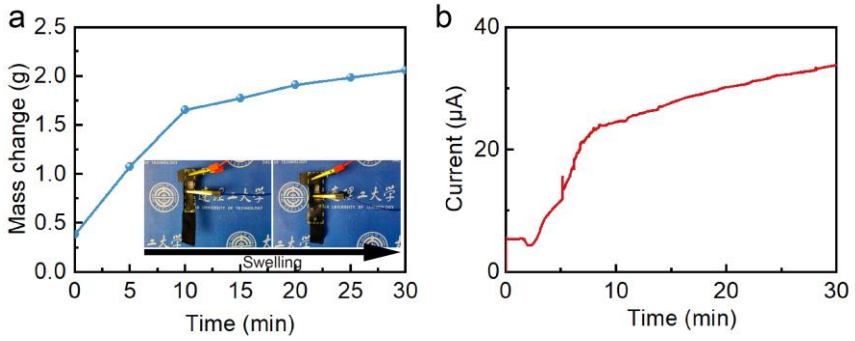

Fig. S8 (a) The mass change of the hydrogel during the swelling process. Inserts are photos of a HEG before and after hydrogel swelling. (b) Corresponding electrical performance during the swelling of hydrogel.

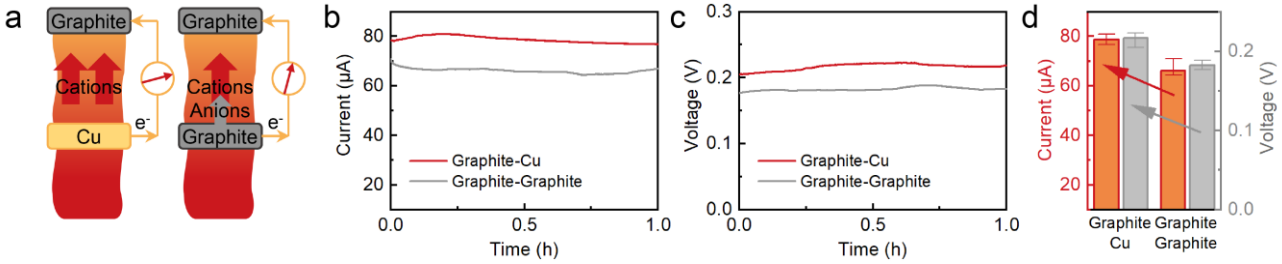

Fig. S9 Effect of the electrodes on electric outputs. (a) Schematic ion migration of different electrode configurations. (b–d) Electric performance and comparison of the two configurations.

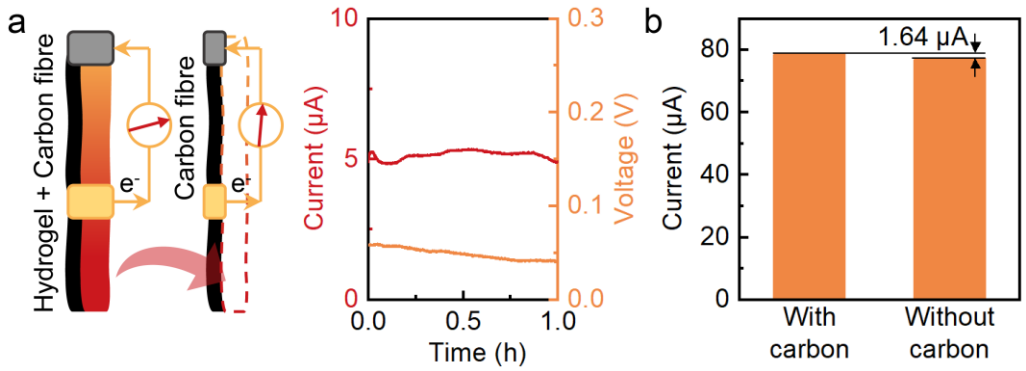

Fig. S10 (a) Contribution of carbon fibre to electric performance. (b) Contribution of carbon to electric performance.

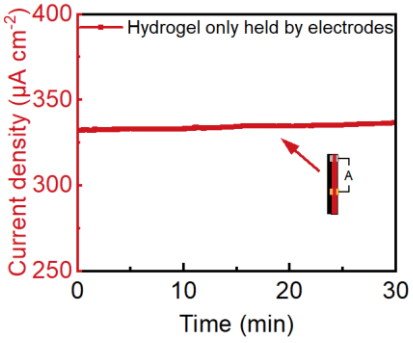

Fig. S11 Current density of the only hydrogel included in a single HEG device.

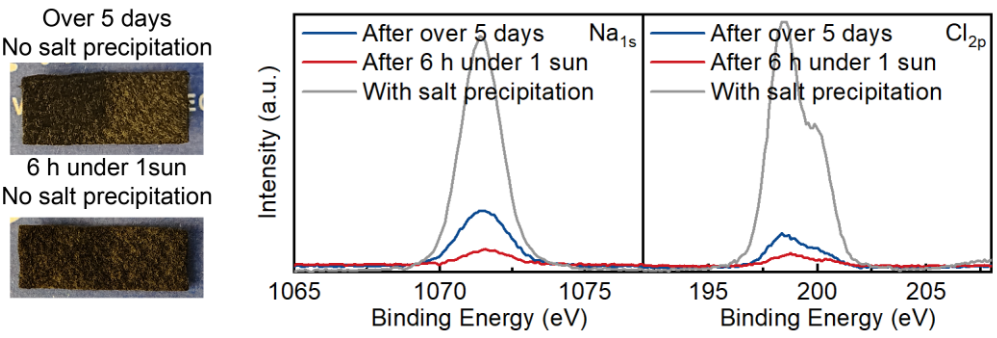

Fig. S12 Photos of graphite electrodes after about 140-hour continuous experiment and a six-hour persistent intense experiment under one-sun irradiation. Comparison of Na and Cl at the electrodes after two tests and the sample with salt precipitation by X-ray photoelectron spectroscopy (XPS). There are no obvious salt crystals observed on the graphite electrodes. The detected Cl is much less than the intensity of the sample with salt.

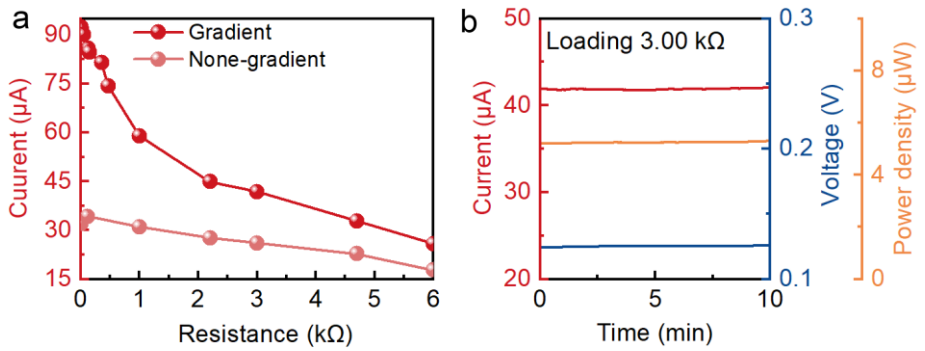

Fig. S13 (a) Output current of HEG with and without an IGC gradient under different load resistance. (b) Electric performance and calculated power of ion-engine HEG with IGC gradient when loading a resistance of 3.00 kΩ.

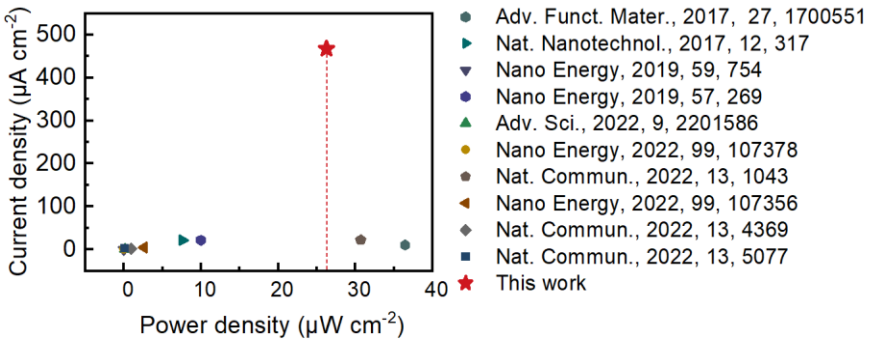

Fig. S14 Comparison of power and current density between the ion-engine HEG and previously reported electricity generators induced by water evaporation. The detailed data correspond to Table S1.

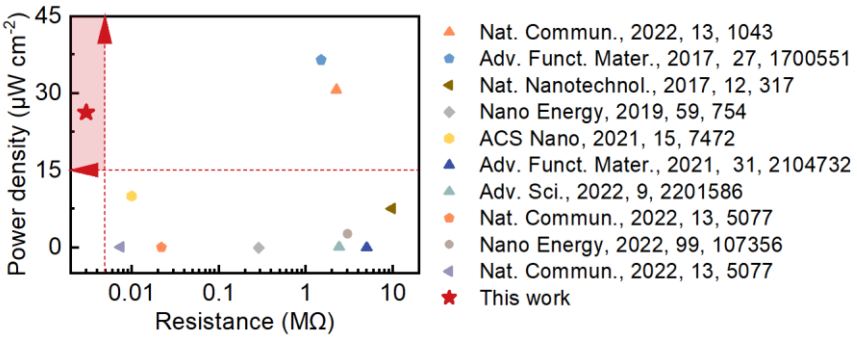

Fig. S15 Comparison of power density and internal resistance between the ion-engine HEG and previously reported electricity generators induced by water evaporation. The detailed data correspond to Table S2.

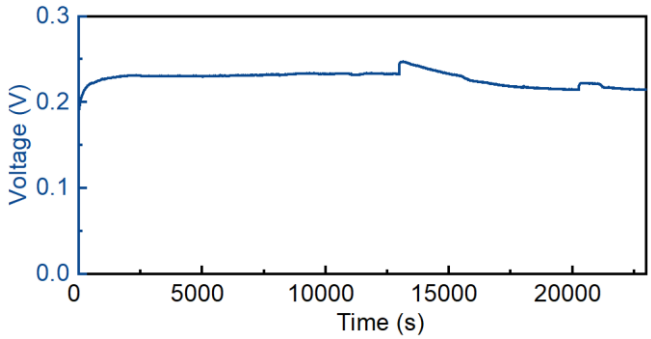

Fig. S16 Open-circuit voltage performance sustained for over 20000 s in salt water under a relative humidity of 45±3% and a room temperature of 25±2℃. The HEG has a size of 5 cm × 1 cm × 0.1 cm.

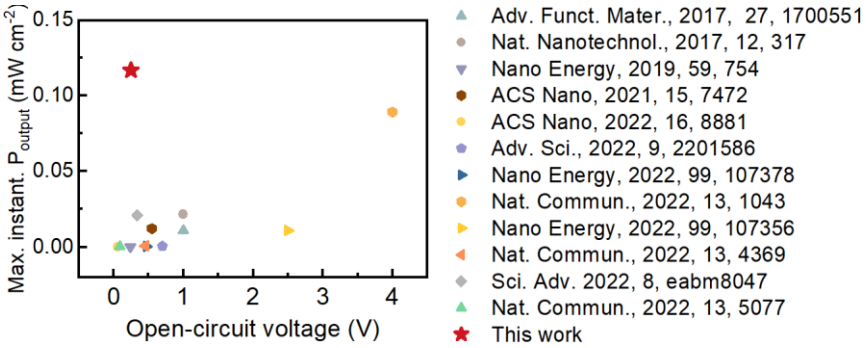

Fig. S17 Comparison of maximum instantaneous output power density and open-circuit voltage between the ion-engine HEG and previously reported electricity generators induced by water evaporation. The detailed data correspond to Table S3. This power density comparison combines the overall performance of open-circuit voltage and short-circuit current and concludes our HEG's better overall performance than other references.

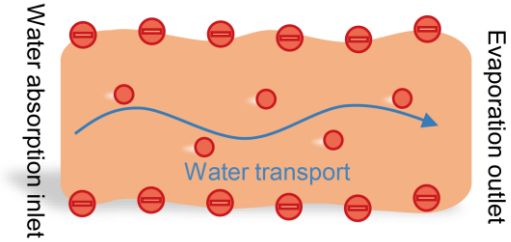

Fig. S18 Schematic mechanism of the typical HEG.

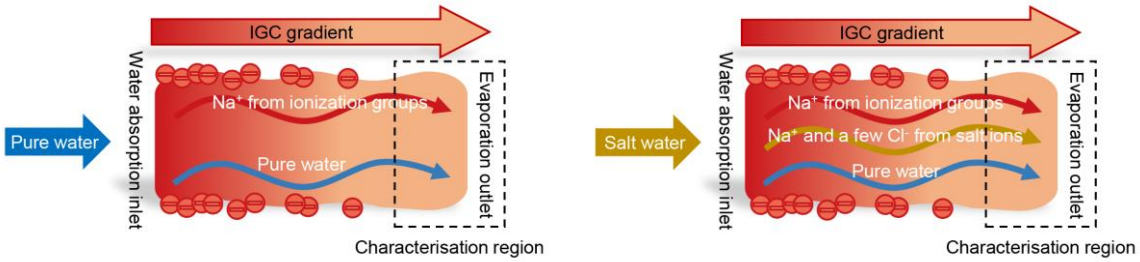

Fig. S19 The schematic diagrams of what ions migrate within the HEG when absorbing pure water and salt water. The dashed boxes are the characterisation regions used for demonstration.

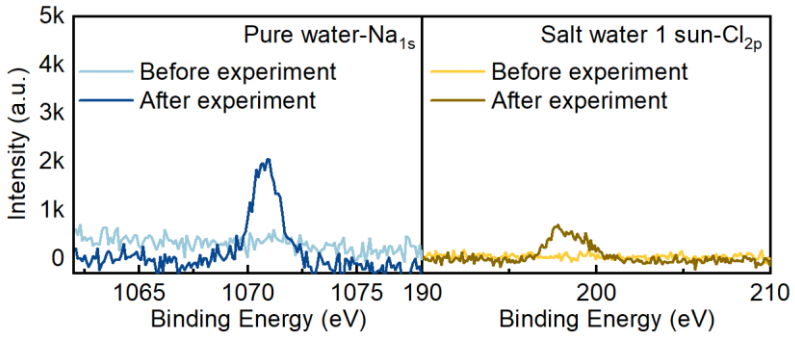

Fig. S20 X-ray photoelectron spectroscopy (XPS) spectra characterising the Na of the evaporation outlet region of this HEG in pure water for three hours and the Cl of the evaporation outlet region of this HEG in salt water for continuous nine hours under 1 sun illumination. We characterised the evaporation outlet region of the HEG before and after the experiments in pure water (the left plot in Fig. S20) and in salt water (the right plot in Fig. S20). The results show that there are almost no Na^+ ions in the evaporation region before the experiment. After a three-hour experiment in pure water, the Na element appeared. Since its source can only be Na^+ in the ionisation groups, it demonstrates that Na^+ in the groups diffuse along the gradient. As there are two sources of Na^+ ions, we used the detection of Cl^- ions to demonstrate that salt ions can migrate in the hydrogel, thus demonstrating that the migrating ions include Na^+ ions from salt ions. It shows after a continuous nine-hour experiment in salt water under 1 sun illumination, a small amount of Cl element was detected, implying that ions in salt water are absorbed and diffuse in the HEG, demonstrating Na^+ from salt ions migrating in the hydrogel.

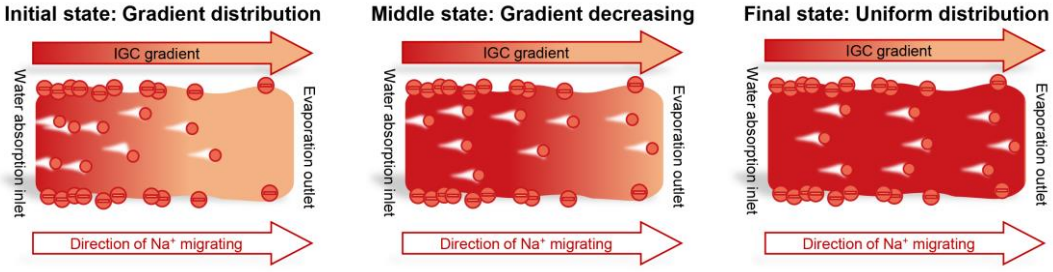

Fig. S21 The schematic diagrams of ion migration in the three states during HEG operation. For ease of understanding, we have divided the Na^+ migration process throughout the current generation into three states for illustration. In the initial state, the Na^+ ions are distributed in a gradient, which is the original state of the hydrogel.

Subsequently, the Na^+ ions migrate toward the evaporation outlet region to generate the current. We refer to this state during the migration process as a middle state. At the final state of migration, the Na^+ ions distribute uniformly in the hydrogel.

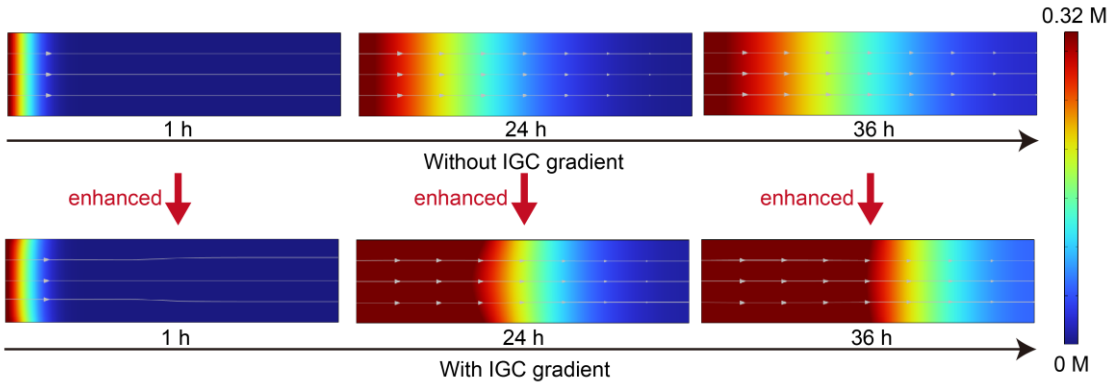

Fig. S22 Simulation of the distribution of Na^+ concentration in the HEG without and with IGC gradient during the operation. We analysed the ion migration process by numerical simulations using COMSOL Multiphysics based on the coupled two-dimensional Nernst-Planck-Poisson (PNP) equations. A 2D model is used for simulating the HEG device. The IGC gradient along the model wall is simplified as a line relationship. The resultant surface charge density, calculated based on the zeta potential, is similarly set as a line relationship. The boundary conditions of the water absorption inlet are set as the constant.

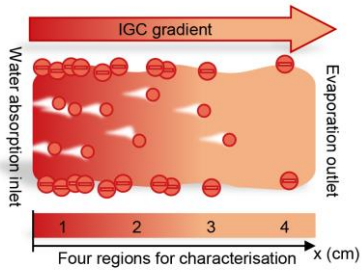

Fig. S23 Schematic demonstration of the four regions used for the Na^+ ion distribution characterisation. The distribution of Na^+ during the migration is characterised based on the above three states. We divided a block of hydrogel into four regions (as illustrated in Fig. S23) and detected each block separately for the element Na.

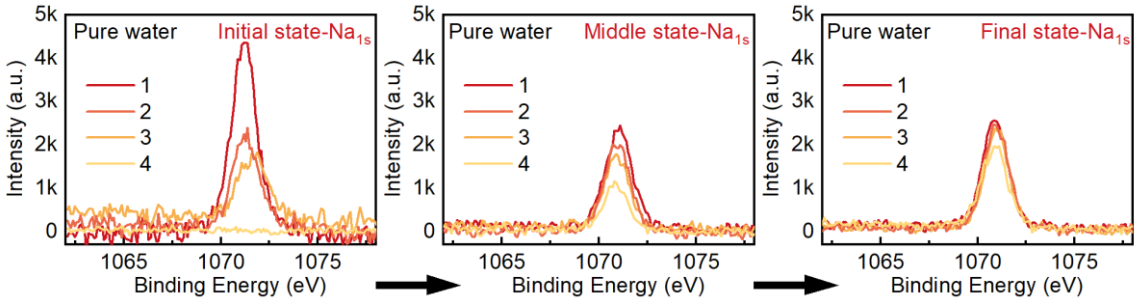

Fig. S24 X-ray photoelectron spectroscopy (XPS) spectra characterising the distribution of Na^+ elements in four regions along the gradient during the three states of the current generation process in pure water. In the initial state, the intensity of Na is a gradient, with region 4 having almost no Na^+ ions and region 1 having significantly

more Na^+ ions than the other three regions, implying the gradient distribution of Na^+ ions in the hydrogel. The middle state shows that the intensity difference between the regions decreases. The Na^+ ions in ionisation groups diffuse into region 4 along the gradient direction. At the final state of the electricity generation, the intensity of Na is nearly uniform.

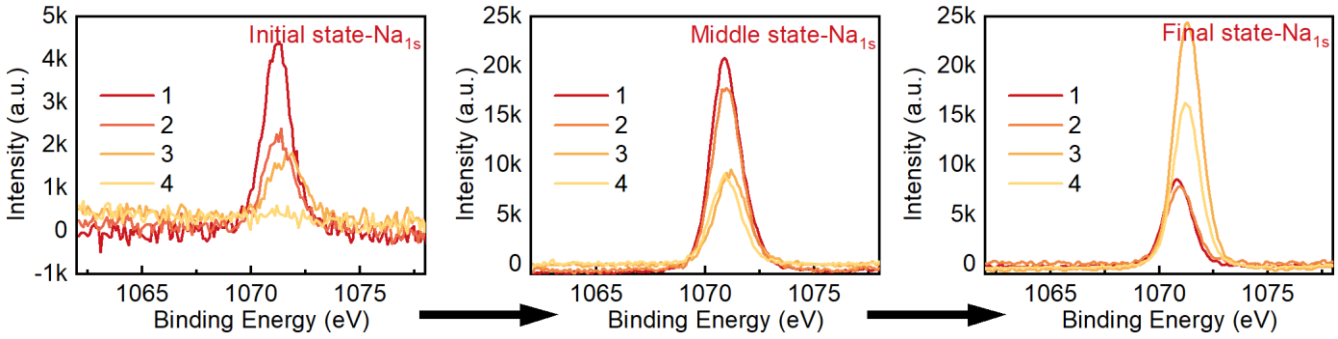

Fig.S25 X-ray photoelectron spectroscopy (XPS) spectra characterising the distribution of Na^+ elements in four regions along the gradient during the three states of the current generation process in salt water. When the HEG operates in salt water, at the middle state, the Na^+ ions in ionisation groups and salt water diffuse along the gradient direction, significantly increasing the corresponding Na^+ content. At the final state, Na^+ ions accumulate on the evaporation outlet region (shown in region 3 and 4 in Fig. S25) because of the continuous entry of salt ions during the operation.

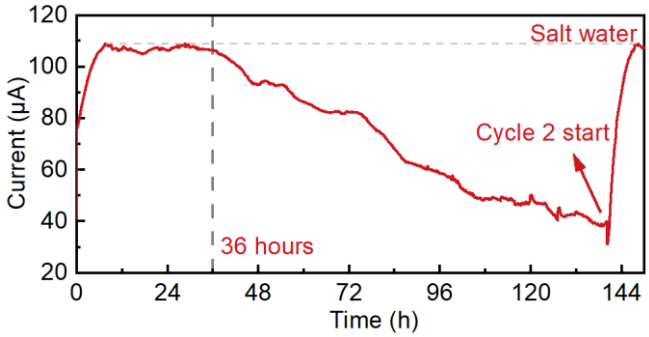

Fig. S26 Current generated by the HEG in salt water for continuous about 140 hours in a single cycle. After Na^+ gradient re-form, the reduced performance returns to the optimum in the cycle 2.

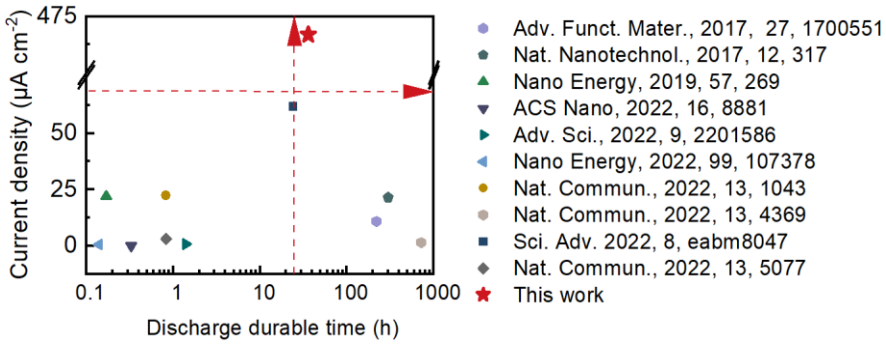

Fig. S27 Comparison of durable time and current density between the ion-engine HEG and previously reported WEGs. The detailed data correspond to Table S4. The durable time is based on the longest durable time reported in the corresponding paper for short-circuit current data, where less than 50s is plotted as 50s. Our discharge time

is maintained at a short-circuit current density ten to one hundred times higher than others, being extremely challenging. In fact, enhancing the current density means the challenge of maintaining a long time[1]. Excitingly, the reduced current density after 140 h is about 200 μA cm^{-2} (40 μA) and still higher than most hydrovoltaic works.

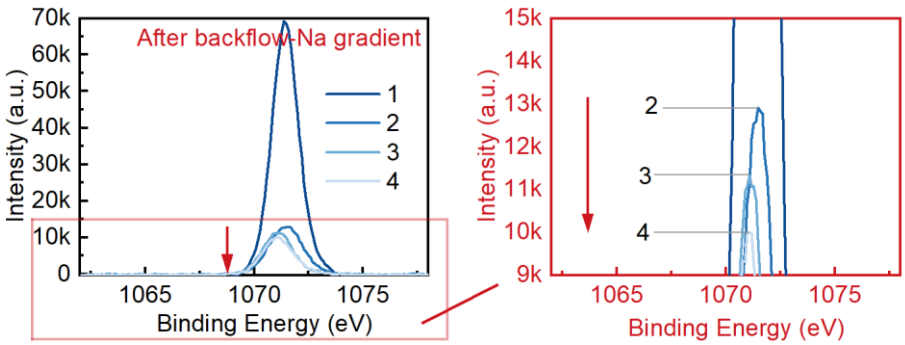

Fig. S28 X-ray photoelectron spectroscopy (XPS) spectra characterising the re-form of a gradient distribution in Na^+ ions after the evaporation surface was covered for eight hours. The enlarged plot indicates that the Na^+ along the region 2 to 4 recovers the gradient distribution. The intensity difference among the three regions is about 1k to 2k, which is similar to that of the initial state (Fig. S25). The reason for the very high intensity of region 1 is that the region is always immersed in salt water and it is possible for the Na^+ ions flowing back from the other three regions to reach region 1.

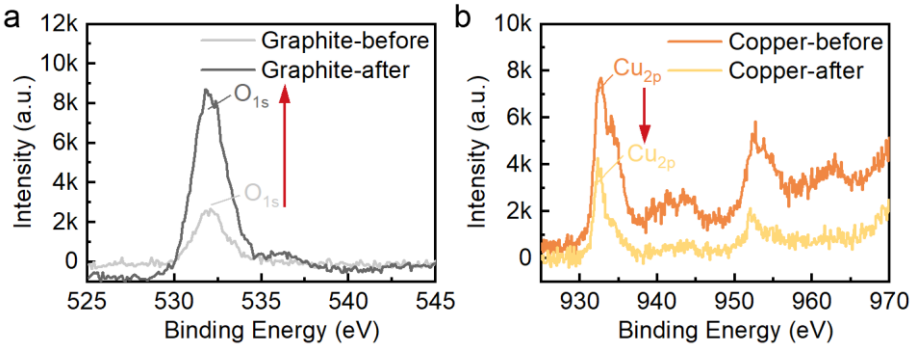

Fig. S29 X-ray photoelectron spectroscopy (XPS) spectra characterising the feature elements of two electrodes before and after experiments, similar to the electrode reactions of metal-air batteries. [2, 3, 4, 5, 6] The conversion from the ion flow to the electron flow can be summarised as follows: In essence, the HEG reasonably enables to yield of directional cation flow, thus producing free electron movement of the external circuit, in which graphite-Cu electrodes participate in the redox reactions to convert an ion flow into an electron flow.

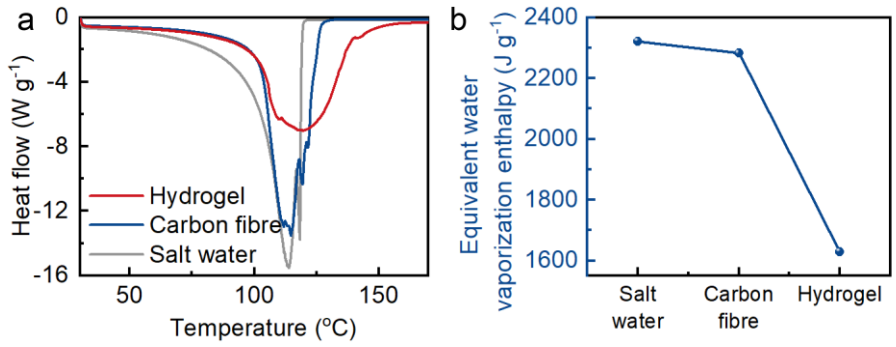

Fig. S30 DSC curves of water evaporation (a) and calculated equivalent water vaporization enthalpy (b) in the hydrogel, in carbon fibre, and in bulk salt water. The measured enthalpy of 3.5wt% salt water is 2322 J g^{-1}, which is very close to the theoretical value of 2364 J g^{-1},[7] indicating the accuracy of our measurements.

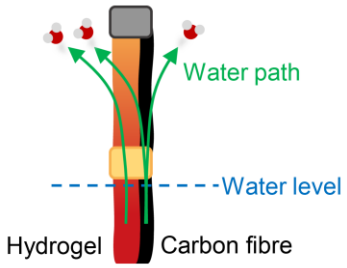

Fig. S31 Schematic of the water flow path in the ion-engine HEG.

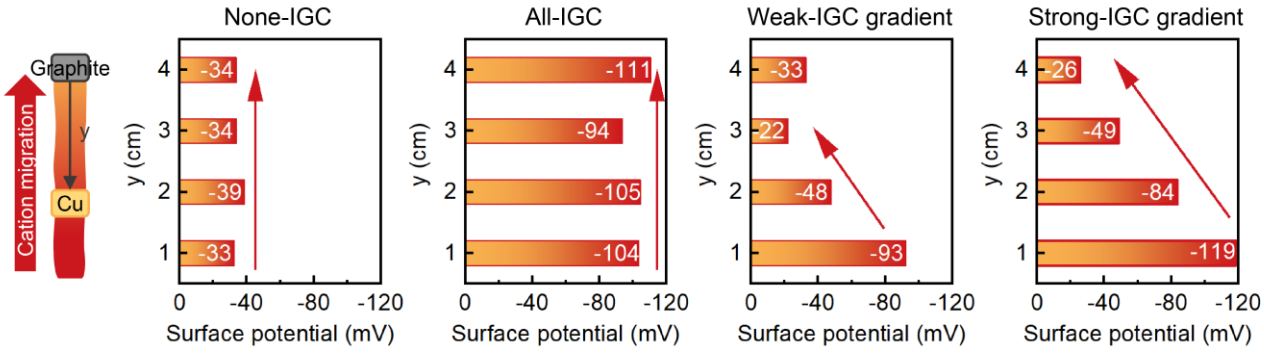

Fig. S32 Mean surface potentials of the KPFM mapping of four regions.

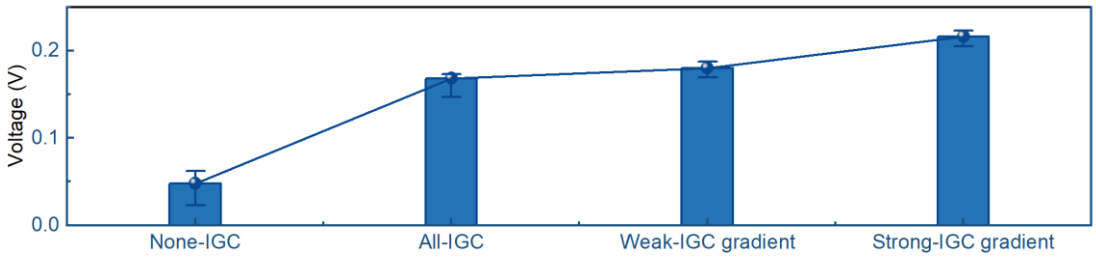

Fig. S33 Voltage performance of the HEGs with different IGC distributions.

The status of the cation hydration state:

The status of the cation hydration state is that the cations are bonded by several water molecules. In this work, the cation refers to the Na^+ ions. According to the previous reports[8, 9, 10, 11], the hydration of Na^+ ions and the formation of hydrogen bonds can weaken the O-H bonds between water molecules. This phenomenon can be detected by Fourier Transform Infrared Spectroscopy (FTIR) measurements. Therefore, FTIR was applied to analyse the status of the hydrated Na^+ state by comparing the spectra of four regions along the gradient (left plot in Fig. S34) with those of pure water (right plot in Fig. S34).

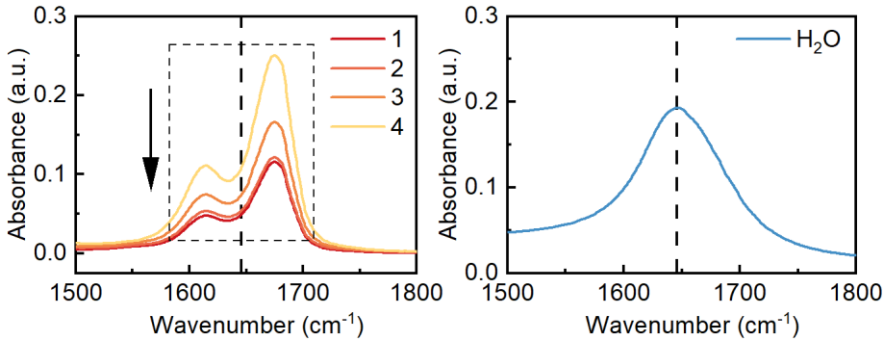

Fig. S34 Fourier Transform Infrared Spectroscopy (FTIR) comparing the spectra of four regions along the gradient with those of pure water.

To eliminate the interference of peaks from free water that are not bonded to Na^+ ions in samples, FTIR was applied by simultaneous acquisition to deduct the response of free water in samples. Compared with the pure water, the O-H bonds peaks at 1646 cm^{-1} are weakened, and the degree of weakening increases from region 4 to region 1 along the ionisation-group concentration gradient. This is consistent with the ionisation-group concentration in the four regions, with region 1 having the highest ionisation group concentration and correspondingly the most Na^+ ions and the strongest weakening of the O-H bond.

Side-by-side comparison of our HEG with recent hydrovoltaic papers including WEGs and MEGs

For making the advancement of this paper clearer over the state-of-the-art, both areal and volumetric power/current density in this work have been side-by-side compared with recent hydrovoltaic papers, as summarised in detail in Table S5. According to the review papers[12], there are two kinds of hydrovoltaic generators, which harvest thermal energy absorbed by water evaporation (WEG) and harvest thermal energy released by moisture condensation (MEG).

Fig. S35 and Fig. S36 indicate that our HEG's current density and power density are higher than most of WEGs (dark colour marks) but not as high as most MEGs (light colour marks). But it is necessary to clarify that our HEG enables a longer durable time compared with the most MEG works with high performance (Fig. S37 and Fig. S38).

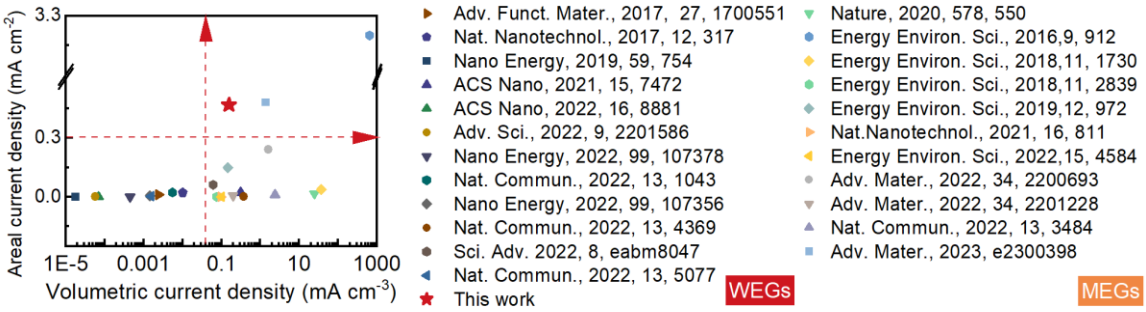

Fig. S35 Comparison of areal and volumetric current density between the ion-engine HEG and previously reported electricity generators including WEGs and MEGs. The detailed data correspond to Table S5.

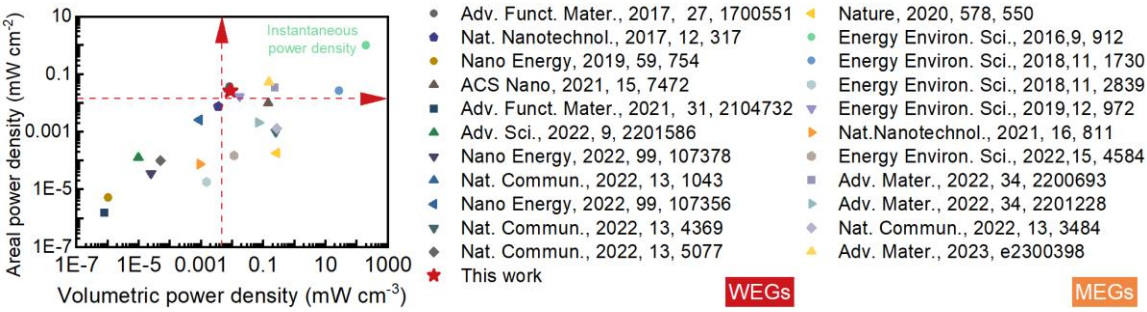

Fig. S36 Comparison of areal and volumetric power density between the ion-engine HEG and previously reported electricity generators including WEGs and MEGs. The detailed data correspond to Table S5.

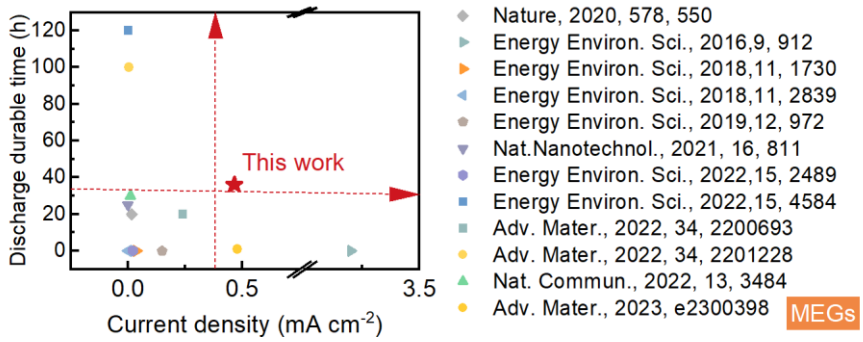

Fig. S37 Comparison of durable time and areal current density between the ion-engine HEG and previously reported MEGs. The detailed data correspond to Table S5. The durable time is based on the longest durable time reported in the corresponding paper for short-circuit current data, where less than 50s is plotted as 50s.

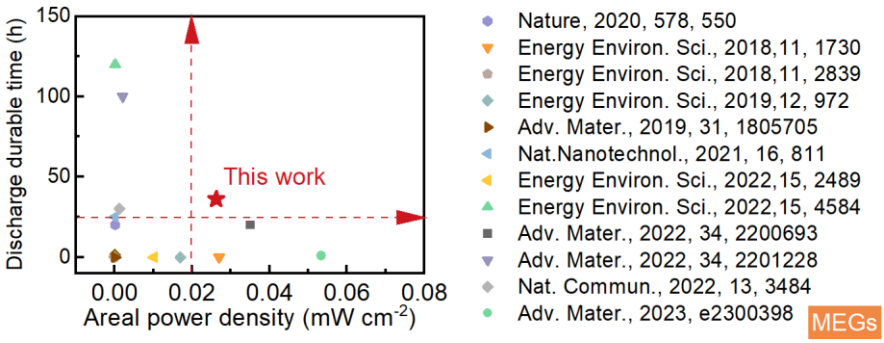

Fig. S38 Comparison of durable time and areal power density between the ion-engine HEG and previously reported MEGs. The detailed data correspond to Table S5. The durable time is based on the longest durable time reported in the corresponding paper for short-circuit current data, where less than 50s is plotted as 50s.

In addition, as an excellent electricity generator, it not only should possess high power density but also has a low internal resistance, ensuring high-performance electricity output to external circuits[11, 13], which is presented as red shade in Fig. S39 and Fig. S40. They indicate that our HEG has a good trade-off between internal resistance and output power density, prior to that of the reported device including WEGs and MEGs. To sum up, this ion-engine HEG possesses state-of-art advantages.

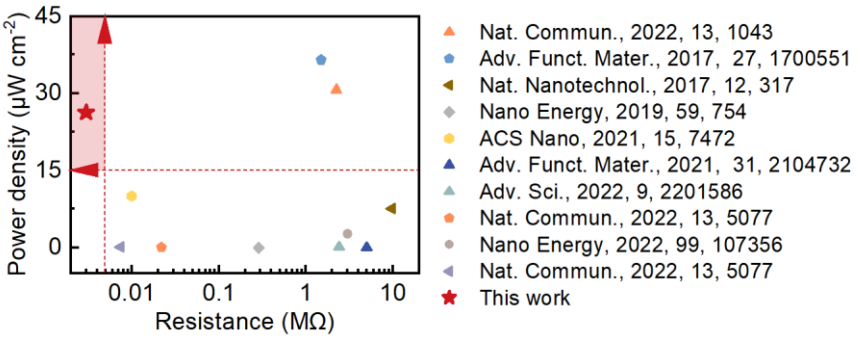

Fig. S39 Comparison of output power density and internal resistance between the ion-engine HEG and previously reported electricity generators induced by water evaporation (WEGs). The detailed data correspond to Table S5.

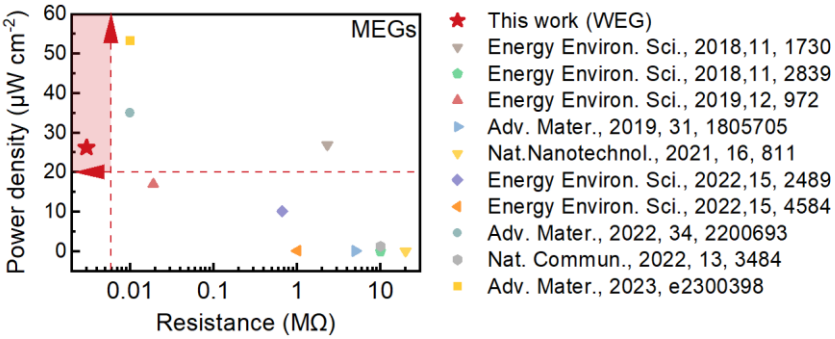

Fig. S40 Comparison of output power density and internal resistance between the ion-engine HEG and previously reported electricity generators induced by moisture (MEGs). The detailed data correspond to Table S5.

Table S1 Summary of power and current density of recently reported hydrovoltaic papers induced by water evaporation. The mentioned density is calculated by the size of the electricity-generating material without electrodes. All data are under dark condition and without wind blowing

Material	**Current density ($\mu A\ cm^{-2}$)**	**Power density ($\mu W\ cm^{-2}$)**	**Ref.**
Printed porous carbon film	10.830	36.450	Adv. Funct. Mater., 2017, 27, 1700551[14]
CB sheet	21.429	7.571	Nat. Nanotechnol., 2017, 12, 317[15]
Kapton board printed carbon ink	0.089	0.005	Nano Energy, 2019, 59, 754[16]
Silicon nanowire	22.000	10.000	ACS Nano, 2021, 15, 7472[2]
Hierarchical Cu (BDC-OH)		0.002	Adv. Funct. Mater., 2021, 31, 2104732[17]
MXene nanosheets	0.070		ACS Nano, 2022, 16, 8881[18]
Al_2O_3 ceramic sheet	0.750	0.127	Adv. Sci., 2022, 9, 2201586[19]

Sugarcane	0.683	0.037	Nano Energy, 2022, 99, 107378[20]
Dual-size Al_2O_3 nanoparticles	22.333	30.667	Nat. Commun., 2022, 13, 1043[21]
Al_2O_3/CB nanoparticles	4.350	2.600	Nano Energy, 2022, 99, 107356[22]
Microbial biofilms	1.500	1.000	Nat. Commun., 2022, 13, 4369[23]
Geobacter sulfurreducens biofilms	62.000		Sci. Adv. 2022, 8, eabm8047[13]
Multi-walled carbon nanotube (MWNT), MXene/$CsPbBr_3$, ionic hydrogel	3.125	0.100	Nat. Commun., 2022, 13, 5077[24]
Ionisation-group concentration gradient in a hydrogel	**466.750**	**26.250**	**This work**

Table S2 Summary of power density and internal resistance of reported hydrovoltaic papers induced by water evaporation. The mentioned density is calculated by the size of the electricity-generating material without electrodes. All data are under dark condition and without wind blowing

Material	**Power density ($\mu W\ cm^{-2}$)**	**Resistance (Ω)**	**Ref.**
Printed porous carbon Film	36.450	1500000	Adv. Funct. Mater., 2017, 27, 1700551[14]
CB sheet	7.571	9660000	Nat. Nanotechnol., 2017, 12, 317[15]
Kapton board printed carbon ink	0.005	288000	Nano Energy, 2019, 59, 754[16]
Ni-Al layered double hydroxide		270000	Nano Energy, 2019, 57, 269[25]
Silicon nanowire	10.000	10000	ACS Nano, 2021, 15, 7472[2]
Hierarchical Cu (BDC-OH)	0.002	5000000	Adv. Funct. Mater., 2021, 31, 2104732[17]
Al_2O_3 ceramic sheet	0.127	2400000	Adv. Sci., 2022, 9, 2201586[19]
Sugarcane	0.037	22000	Nano Energy, 2022, 99, 107378[20]
Dual-size Al_2O_3 nanoparticles	30.667	2220000	Nat. Commun., 2022, 13, 1043[21]
Al_2O_3/CB nanoparticles	2.600	3000000	Nano Energy, 2022, 99, 107356[22]
Microbial biofilms	1.000		Nat. Commun., 2022, 13, 4369[23]
Multi-walled carbon nanotube (MWNT), MXene/$CsPbBr_3$, ionic hydrogel	0.100	7460	Nat. Commun., 2022, 13, 5077[24]
Ionisation-group concentration gradient in a hydrogel	**26.250**	**3000**	**This work**

Table S3 Summary of open-circuit voltage and maximum instantaneous output power density of reported hydrovoltaic papers induced by water evaporation. The mentioned density is calculated by the size of the electricity-generating material without electrodes. All data are under dark condition and without wind blowing

Material	Current density (μA cm^{-2})	Open-circuit voltage (V)	Maximum instantaneous output power density (μW cm^{-2})	Ref.
Printed porous carbon film	10.830	1.000	10.830	Adv. Funct. Mater., 2017, 27, 1700551[14]
CB sheet	21.429	1.000	21.429	Nat. Nanotechnol., 2017, 12, 317[15]
Kapton board printed carbon ink	0.089	0.239	0.021	Nano Energy, 2019, 59, 754[16]
Ni-Al layered double hydroxide		0.700		Nano Energy, 2019, 57, 269[25]
Silicon nanowire	22.000	0.550	12.100	ACS Nano, 2021, 15, 7472[2]
Hierarchical Cu (BDC-OH)		0.600		Adv. Funct. Mater., 2021, 31, 2104732[17]
MXene nanosheets	0.070	0.061	0.004	ACS Nano, 2022, 16, 8881[18]
Al_2O_3 ceramic sheet	0.750	0.700	0.525	Adv. Sci., 2022, 9, 2201586[19]
Sugarcane	0.683	0.470	0.321	Nano Energy, 2022, 99, 107378[20]
Dual-size Al_2O_3 nanoparticles	22.333	4.000	89.333	Nat. Commun., 2022, 13, 1043[21]
Al_2O_3/CB nanoparticles	4.350	2.500	10.875	Nano Energy, 2022, 99, 107356[22]
Microbial biofilms	1.500	0.450	0.675	Nat. Commun., 2022, 13, 4369[23]
Geobacter sulfurreducens biofilms	62.000	0.340	21.080	Sci. Adv. 2022, 8, eabm8047[13]
Multi-walled carbon nanotube (MWNT), MXene/$CsPbBr_3$, ionic hydrogel	3.125	0.090	0.281	Nat. Commun., 2022, 13, 5077[24]
Ionisation-group concentration gradient in a hydrogel	**466.750**	**0.250**	**116.688**	**This work**

Table S4 Summary of discharge durable time and current density of recently reported hydrovoltaic papers induced by water evaporation. The mentioned density is calculated by the size of the electricity-generating material without electrodes. All data are under dark condition and without wind blowing

Material	Current density (μA cm^{-2})	Discharge durable time (h)	Ref.
Printed porous carbon film	10.830	220	Adv. Funct. Mater., 2017, 27, 1700551[14]
CB sheet	21.429	300	Nat. Nanotechnol., 2017, 12, 317[15]
Kapton board printed carbon ink	0.089		Nano Energy, 2019, 59, 754[16]
Ni-Al layered double hydroxide		12	Nano Energy, 2019, 57, 269[25]
Silicon nanowire	22.000	0.17	ACS Nano, 2021, 15, 7472[2]
Hierarchical Cu(BDC-OH)		0.19	Adv. Funct. Mater., 2021, 31, 2104732[17]
MXene nanosheets	0.070	0.33	ACS Nano, 2022, 16, 8881[18]
Al_2O_3 ceramic sheet	0.750	1.39	Adv. Sci., 2022, 9, 2201586[19]
Sugarcane	0.683	0.14	Nano Energy, 2022, 99, 107378[20]
Dual-size Al_2O_3 nanoparticles	22.333	0.83	Nat. Commun., 2022, 13, 1043[21]
Al_2O_3/CB nanoparticles	4.350		Nano Energy, 2022, 99, 107356[22]
Microbial biofilms	1.500	720	Nat. Commun., 2022, 13, 4369[23]
Geobacter sulfurreducens biofilms	62.000	24	Sci. Adv. 2022, 8, eabm8047[13]
Multi-walled carbon nanotube (MWNT), MXene/$CsPbBr_3$, ionic hydrogel	3.125	0.83	Nat. Commun., 2022, 13, 5077[24]
Ionisation-group concentration gradient in a hydrogel	**466.750**	**36**	**This work**

Table S5 Summary of both areal and volumetric power/current density of recently reported hydrovoltaic papers. The mentioned density is calculated by the size of the electricity-generating material without electrodes. All data are under dark condition and without wind blowing

	Material	Areal current density (μA cm^{-2})	Volumetric current density (μA cm^{-3})	Areal power density (μW cm^{-2})	Volumetric power density (μW cm^{-3})	Discharge durable time (h)	Resistance (Ω)	Ref.
Water evaporation-induced electricity generator (WEG)	Printed porous carbon film	10.830	2.407	36.450	8.100	220	1500000	Adv. Funct. Mater., 2017, 27, 1700551[14]
	CB sheet	21.429	10.204	7.571	3.605	300	9660000	Nat. Nanotechnol., 2017, 12, 317[15]
	Kapton board printed carbon ink	0.089	0.018	0.005	0.001		288000	Nano Energy, 2019, 59, 754[16]

	Ni-Al layered double hydroxide				16.100	12	270000	Nano Energy, 2019, 57, 269[25]
	Silicon nanowire	22.000	314.286	10.000	142.857	600s	10000	ACS Nano, 2021, 15, 7472[2]
	Hierarchical Cu (BDC-OH)			0.002	0.001	700s	5000000	Adv. Funct. Mater., 2021, 31, 2104732[17]
	MXene nanosheets	0.070	0.070			20min		ACS Nano, 2022, 16, 8881[18]
	Al_2O_3 ceramic sheet	0.750	0.058	0.127	0.010	5000s	2400000	Adv. Sci., 2022, 9, 2201586[19]
	Sugarcane	0.683	0.456	0.037	0.024	500s	22000	Nano Energy, 2022, 99, 107378[20]
	Dual-size Al_2O_3 nanoparticles	22.333	5.583	30.667	7.667	50min	2220000	Nat. Commun., 2022, 13, 1043[21]
	Al_2O_3/CB nanoparticles	4.350	1.450	2.600	0.867		3000000	Nano Energy, 2022, 99, 107356[22]
	Microbial biofilms	1.500	375.000	1.000	250.000	720		Nat. Commun., 2022, 13, 4369[23]
	Geobacter sulfurreducens biofilms	62.000	62.000			24		Sci. Adv. 2022, 8, eabm8047[13]
	Multi-walled carbon nanotube (MWNT), MXene/$CsPbBr_3$, ionic hydrogel	3.125	1.563	0.100	0.050	3000s	7460	Nat. Commun., 2022, 13, 5077[24]
This work (WEG)	**Ionisation-group concentration gradient in a hydrogel**	**466.750**	**155.583**	**26.250**	**8.750**	**36**	**3000**	**This work**
Moisture-induced electricity generator (MEG)	Protein nanowires	17.000	24285.714	0.186	266.000	20		Nature, 2020, 578, 550[26]
	Graphene oxide frameworks	3200.000	640000.000	1000.000 (instantaneous)	200000.000 (instantaneous)			Energy Environ. Sci., 2016,9, 912[27]
	Graphene oxide		85.000		11.100		10000000	Nat. Commun., 2018, 9, 4166[28]
	Graphene oxide (GO) onto a moisture insulation substrate (MIS)	37.037	37037.037	27.000	27000.000	＜50 s	2300000	Energy Environ. Sci., 2018,11, 1730[29]
	Graphene oxide membrane	0.900	75.000	0.018	1.500		10000000	Energy Environ. Sci., 2018,11, 2839[30]
	Polyelectrolyte membrane of poly (4-styrensulfonic acid) (PSSA)	150.000	150.000	17.000	17.000		19000	Energy Environ. Sci., 2019,12, 972[31]
	Graphene oxide film			0.102			5000000	Adv. Mater., 2019, 31, 1805705[32]

Bilayer polyelectrolyte films	0.080	96.000	0.076	0.900	＜25	20000000	Nat. Nanotechnol., 2021, 16, 811[33]
Ionic polymer–hydrogel–carbon composite	21.800		10.140		200s	660000	Energy Environ. Sci., 2022,15, 2489[34]
Electrospun nanofiber film	1.333	101.010	0.150	11.400	120	1000000	Energy Environ. Sci., 2022,15, 4584[35]
Ionic hydrogel	240.000	1600.000	35.000	233.333	20	10000	Adv. Mater., 2022, 34, 2200693[36]
Ionic hydrogel on carbon	6.000	200.000	2.100	70.000	100		Adv. Mater., 2022, 34, 2201228[37]
CNT-metal electrodes, and AAO	11.300	2407.769	1.300	277.000	<30	10000000	Nat. Commun., 2022, 13, 3484[6]
LiCl and ionic hydrogel	480.000	1371.429	53.300	152.286	1	10000	Adv. Mater., 2023, e2300398[38]

1. P. Shi, X. B. Cheng, T. Li, R. Zhang, H. Liu, C. Yan, X. Q. Zhang, J. Q. Huang and Q. Zhang, *Adv Mater*, 2019, **31**, e1902785.
2. B. Shao, Z. Song, X. Chen, Y. Wu, Y. Li, C. Song, F. Yang, T. Song, Y. Wang, S. T. Lee and B. Sun, *ACS Nano*, 2021, **15**, 7472-7481.
3. K. Zhang, L. Cai, A. Nilghaz, G. Chen, X. Wan and J. Tian, *Nano Energy*, 2022, **98**, 107288.
4. Y. Qin, Y. Wang, X. Sun, Y. Li, H. Xu, Y. Tan, Y. Li, T. Song and B. Sun, *Angew Chem Int Ed Engl*, 2020, **59**, 10619-10625.
5. V.-H. Trinh, N.-A. Nguyen, O. Omelianovych, V.-D. Dao, I. Yoon, H.-S. Choi and M. Keidar, *Desalination*, 2022, **535**, 115820.
6. Y. Zhang, T. Yang, K. Shang, F. Guo, Y. Shang, S. Chang, L. Cui, X. Lu, Z. Jiang, J. Zhou, C. Fu and Q. C. He, *Nat Commun*, 2022, **13**, 3484.
7. M. H. Sharqawy, J. H. Lienhard and S. M. Zubair, *Desalination Water Treat.*, 2012, **16**, 354.
8. J. Peng, D. Cao, Z. He, J. Guo, P. Hapala, R. Ma, B. Cheng, J. Chen, W. J. Xie, X. Z. Li, P. Jelinek, L. M. Xu, Y. Q. Gao, E. G. Wang and Y. Jiang, *Nature*, 2018, **557**, 701-705.
9. P. Wang, R. Shi, Y. Su, L. Tang, X. Huang and J. Zhao, *Front Chem*, 2019, **7**, 624.
10. Dorothy J. Miller and J. M. Lisy, *J. Am. Chem. Soc.*, 2008, **130**, 15381–15392.
11. H. Wang, T. He, X. Hao, Y. Huang, H. Yao, F. Liu, H. Cheng and L. Qu, *Nat. Commun.*, 2022, **13**, 2524.
12. D. Shen, W. W. Duley, P. Peng, M. Xiao, J. Feng, L. Liu, G. Zou and Y. N. Zhou, *Adv Mater*, 2020, **32**, e2003722.
13. Qichang Hu, Yongji Ma, Guoping Ren, Bintian Zhang and S. Zhou, *Sci. Adv.*, 2022, **8**, eabm8047.
14. T. Ding, K. Liu, J. Li, G. Xue, Q. Chen, L. Huang, B. Hu and J. Zhou, *Adv. Funct. Mater.*, 2017, **27**, 1700551.
15. G. Xue, Y. Xu, T. Ding, J. Li, J. Yin, W. Fei, Y. Cao, J. Yu, L. Yuan, L. Gong, J. Chen, S. Deng, J. Zhou and W. Guo, *Nat. Nanotechnol.*, 2017, **12**, 317-321.
16. H. Guan, T. Zhong, H. He, T. Zhao, L. Xing, Y. Zhang and X. Xue, *Nano Energy*, 2019, **59**, 754-761.
17. Z. Wang, Y. Wu, K. Xu, L. Jiang, J. Sun, G. Cai, G. Li, B. Y. Xia and H. Liu, *Adv. Funct. Mater.*, 2021, **31**, 2104732.
18. X. Che, W. Zhang, L. Long, X. Zhang, D. Pei, M. Li and C. Li, *ACS Nano*, 2022, **16**, 8881-8890.
19. J. Chi, C. Liu, L. Che, D. Li, K. Fan, Q. Li, W. Yang, L. Dong, G. Wang and Z. L. Wang, *Adv. Sci.*, 2022, **9**, 2201586.
20. H. Li, X. Li, X. Li, H. Wang, J. Huang, S. K. Boong, H. K. Lee, J. Han and R. Guo, *Nano Energy*, 2022, **99**.

21. L. Li, S. Feng, Y. Bai, X. Yang, M. Liu, M. Hao, S. Wang, Y. Wu, F. Sun, Z. Liu and T. Zhang, *Nat. Commun.*, 2022, **13**, 1043.
22. L. Li, S. Feng, L. Du, Y. Wang, C. Ge, X. Yang, Y. Wu, M. Liu, S. Wang, Y. Bai, F. Sun and T. Zhang, *Nano Energy*, 2022, **99**, 107356.
23. X. Liu, T. Ueki, H. Gao, T. L. Woodard, K. P. Nevin, T. Fu, S. Fu, L. Sun, D. R. Lovley and J. Yao, *Nat. Commun.*, 2022, **13**, 4369.
24. Z. Sun, C. Han, S. Gao, Z. Li, M. Jing, H. Yu and Z. Wang, *Nat Commun*, 2022, **13**, 5077.
25. J. Sun, P. Li, J. Qu, X. Lu, Y. Xie, F. Gao, Y. Li, M. Gang, Q. Feng, H. Liang, X. Xia, C. Li, S. Xu and J. Bian, *Nano Energy*, 2019, **57**, 269-278.
26. X. Liu, H. Gao, J. E. Ward, X. Liu, B. Yin, T. Fu, J. Chen, D. R. Lovley and J. Yao, *Nature*, 2020, **578**, 550-554.
27. F. Zhao, Y. Liang, H. Cheng, L. Jiang and L. Qu, *Energy Environ. Sci.*, 2016, **9**, 912-916.
28. Y. Huang, H. Cheng, C. Yang, P. Zhang, Q. Liao, H. Yao, G. Shi and L. Qu, *Nat Commun*, 2018, **9**, 4166.
29. Y. Liang, F. Zhao, Z. Cheng, Y. Deng, Y. Xiao, H. Cheng, P. Zhang, Y. Huang, H. Shao and L. Qu, *Energy Environ. Sci.*, 2018, **11**, 1730-1735.
30. H. Cheng, Y. Huang, F. Zhao, C. Yang, P. Zhang, L. Jiang, G. Shi and L. Qu, *Energy Environ. Sci.*, 2018, **11**, 2839-2845.
31. T. Xu, X. Ding, Y. Huang, C. Shao, L. Song, X. Gao, Z. Zhang and L. Qu, *Energy Environ. Sci.*, 2019, **12**, 972-978.
32. C. Yang, Y. Huang, H. Cheng, L. Jiang and L. Qu, *Adv Mater*, 2019, **31**, e1805705.
33. H. Wang, Y. Sun, T. He, Y. Huang, H. Cheng, C. Li, D. Xie, P. Yang, Y. Zhang and L. Qu, *Nat. Nanotechnol.*, 2021, **16**, 811-819.
34. C. Liu, S. Wang, X. Wang, J. Mao, Y. Chen, N. X. Fang and S.-P. Feng, *Energy Environ. Sci.*, 2022, **15**, 2489-2498.
35. Z. Sun, X. Wen, L. Wang, J. Yu and X. Qin, *Energy Environ. Sci.*, 2022, **15**, 4584-4591.
36. S. Yang, X. Tao, W. Chen, J. Mao, H. Luo, S. Lin, L. Zhang and J. Hao, *Adv Mater*, 2022, **34**, e2200693.
37. Y. Zhang, S. Guo, Z. G. Yu, H. Qu, W. Sun, J. Yang, L. Suresh, X. Zhang, J. J. Koh and S. C. Tan, *Adv Mater*, 2022, **34**, e2201228.
38. H. Zhang, N. He, B. Wang, B. Ding, B. Jiang, D. Tang and L. Li, *Adv Mater*, 2023, DOI: 10.1002/adma.202300398, e2300398.